TUDelft

Delft University of Technology

High dielectric filler for all-solid-state lithium metal battery

Wang, Chao; Liu, Ming; Bannenberg, Lars J.; Zhao, Chenglong; Thijs, Michel; Boshuizen, Bart; Ganapathy, Swapna; Wagemaker, M.

Important note
To cite this publication, please use the final published version (if applicable).
Please check the document version above.

High dielectric filler for all-solid-state lithium metal battery

Chao Wang [a,d,*], Ming Liu [a], Lars J. Bannenberg [a], Chenglong Zhao [a], Michel Thijs [b], Bart Boshuizen [c], Swapna Ganapathy [a], Marnix Wagemaker [a,**]

[a] Storage of Electrochemical Energy, Radiation Science and Technology, Faculty of Applied Sciences, Delft University of Technology, the Netherlands
[b] Neutron & Positron Methods for Materials, Radiation Science and Technology, Faculty of Applied Sciences, Delft University of Technology, the Netherlands
[c] Department of Chemical Engineering, Faculty of Applied Sciences, Delft University of Technology, the Netherlands
[d] Department of Applied Biology and Chemical Technology, The Hong Kong Polytechnic University, Hong Kong Special Administrative Region

HIGHLIGHTS

- Dendrite growth in solid Li metal cell is alleviated with a dielectric material.
- $BaTiO_3$ removes the electric field gradients that catalyze dendrite formation.
- Small over-potential of 48 mV was obtained at 1 mA/cm^2 in symmetric cell.
- Solid-state NMR and XPS measurements show eliminated electrolyte decomposition.
- Reducing solid electrolyte decomposition results in improved cycling efficiency.

ARTICLE INFO

ABSTRACT

Lithium metal with its high theoretical capacity and low negative potential is considered one of the most important candidates to raise the energy density of all-solid-state batteries. However, lithium filament growth and its induced solid electrolyte decomposition pose severe challenges to realize a long cycle life. Here, dendrite growth in solid-state Li metal batteries is alleviated by introducing a high dielectric material, barium titanate, as a filler that removes the electric field gradients that catalyze dendrite formation. In symmetrical Li-metal cells, this results in a very small over-potential of only 48 mV at a relatively high current density of 1 mA cm^{-2}, when cycling a capacity of 2 mA h cm^{-2} during 1700 h. The high dielectric filler improves the Coulombic efficiency and cycle life of full cells and suppresses electrolyte decomposition as indicated by solid-state nuclear magnetic resonance (NMR) and X-ray photoelectron spectroscopy (XPS) measurements. This indicates that the high dielectric filler can suppress dendrite formation, thereby reducing solid electrolyte decomposition reactions, resulting in the observed low overpotentials and improved cycling efficiency.

1. Introduction

With the development of electric mobility, the requirements for battery energy density and safety are rapidly rising [1,2]. State-of-the-art liquid-based batteries pose leakage and fire hazard risks [3–5]. The solid-state battery is a promising candidate for next-generation battery design being intrinsically safer, however, so far the practical energy density is lower as compared with liquid-based batteries [6,7]. In theory, the energy density of solid-state batteries

may be increased significantly by replacing graphite with a lithium-metal anode which has a theoretical specific capacity of 3860 mA g^{-1} [8].

However, there are two interlinked challenges with Li-metal anodes: (i) inhomogeneous lithium metal deposition upon charging that drives dendrite formation, ultimately resulting in a short-circuit, and (ii) electrolyte decomposition due to the strongly reducing potentials of Li-metal [8–12]. Initially the hope was that solid electrolytes, replacing liquid ones, could prevent both detrimental processes through their high

---

shear modulus in comparison to that of Li-metal and the expected higher electrochemical stability. However, research has demonstrated that both factors present formidable challenges for Li-metal solid-state batteries. For example, in situ X-ray tomography provides direct evidence that lithium dendrites/filaments tend to grow along with the grains and grain boundaries of the inorganic solid-state electrolyte [13–15], demonstrating that inhomogeneous lithium metal deposition causes short-circuiting even in solid-state batteries [13,16].

The mechanism of dendrite growth is very different in solid electrolytes as compared to liquid electrolytes [17], where one important factor appears to be the applied pressure that typically exceeds the yield strength of Li-metal (~0.8 MPa). Dendrite growth is believed to be induced by preferential deposition on local inhomogeneities like grain boundaries and voids present at the Li-metal electrolyte interfaces. This deposition results in local hotspots of high currents. In combination with the much larger molar volume of Li-metal as compared to Li in solid electrolytes [18], these hotspots have been suggested to cause local expansion that ultimately causes cracks filled with Li metal deposits [19]. The quick polarization before a real short circuit of solid-state batteries [20] and the generally observed rise in battery polarization [21] underline the interlinked problem that most solid electrolytes are not stable towards the low reduction potential of Li-metal. Indeed, most solid electrolytes are predicted to be unstable towards Li-metal [21,22], which is especially exposed through the high surface area of dendrite filaments in solid-state batteries.

Strategies that have been explored to suppress dendrite formation include enhancing the Li-ion mobility and/or reducing the local current density [23–31], minimizing interfacial inhomogeneities [32], increasing the adhesion by improving the wettability of Li-metal [24], and design of solid electrolyte interfaces (SEI) [23] and buffer layers [24] to promote interface adhesion and homogeneity. One of the fundamental drivers for dendrite growth is considered to be the focusing electrical field lines at sharp features, caused by the larger surface charge density [33]. Based on this we investigate the introduction of a high dielectric material as filler to reduce the electric field gradients as an alternative approach to suppress dendrites. The high polarizing power of a high dielectric establishes an effective immobile surface (space) charge density ρ_{charge} that opposes the applied field in the battery and scales with the dielectric constant ($\nabla \bullet D = \rho_{charge}$ where $D = \varepsilon_0\varepsilon_r E$, ε_0 and ε_r the vacuum and relative permittivity and E the electrical field). Dictated by Gauss Law, the electrical field lines focus towards the high dielectric additive that, when positioned in between dielectric materials, lowers the divergence of the electrical field at the tip of a dendrite near a high dielectric material. Although the actual conditions, including a specific current density and local environment that, can enhance the local electrical field gradient, the presence of a high dielectric can by hypothesised to suppress dendrite formation.

To introduce a high dielectric filler that mitigates dendrite formation in practice, barium titanate is added to both the Li-metal electrode and solid sulfide electrolyte of a solid-state battery. Barium titanate was selected as it combines a high (relative) dielectric constant ($\varepsilon_r = 4000$) with electrochemical stability towards Li. The experimental results show that the introduction of the filler improves electrochemical performance. Symmetrical Li-metal cycling with the high dielectric filler particles results in a low overpotential of only 48 mV at 1 mA cm^{-2}, cycling a capacity of 2 mA h cm^{-2} capacity during 1700 h. This composite anode has a specific capacity of 504 mA h g^{-1}, taking into account the mass of both Li-metal and the dielectric material in the Li-metal anode. We demonstrate that the high permittivity of the filler suppresses dendrite growth, promoting homogeneous plating (electrochemical Li metal deposition), thereby damping the self-amplifying cycle of electrolyte decomposition and dendritic growth. Moreover, this high dielectric filler increases the Coulombic efficiency and cycle life in full cells. Electrolyte decomposition is shown to be reduced, as testified by X-ray photoelectron spectroscopy and solid-state NMR experiments,

rationalizing the improved performances. Thereby, the high dielectric concept is suggested to impact electrochemical Li metal deposition, such that it suppresses dendrite formation and improves the cycle life of solid-state batteries.

2. Results and discussion

2.1. Electric field calculations

Before the experimental evaluation of the effect of adding dielectric particles in the Li-metal and/or solid-state electrolyte on the electrochemical performance and formation of decomposition products, we first illustrate how the electric field gradients are affected by the introduction of these additives. This is achieved by computing the electric field in two dimensions in the voltage range of 0–1 V using COMSOL Multiphysics 5.5 for different symmetric cell configurations. Dendritic features are represented by rectangular-shaped Li-metal inhomogeneities (1 μm × 2 μm) with a hemispherical tip. The dielectric additives are modeled as spherical particles with sizes between 1 and 8 μm to represent the practical situation evaluated experimentally in this study. We investigate the impact of the magnitude of the dielectric constant by comparing BaTiO$_3$ (BTO) with Al$_2$O$_3$ (AO) particles that have a dielectric constant of $\varepsilon_r = 4000$ and 8, respectively. As such, the dielectric constant of AO only slightly exceeds that of the Li$_6$PS$_5$Cl (LPSC) solid electrolyte ($\varepsilon_r = 5$). It should be noted that these simulations present strongly simplified conditions not taking into account the piezoelectrical effect of BTO and modulation of the electrical field gradients due to the dynamic conditions (current density) as well as due to the double layer are neglected (both increasing the local electrical field gradients). As set out in Experimental 4.6, the electrical field gradients under static conditions are estimated to be relatively large, thus providing at least a qualitative indication of the impact of dielectric volumes in the vicinity of dendrites.

Fig. 1 and Fig. S1 present the computational results for four cell configurations: (1) Li-metal electrodes combined with LPSC as solid electrolyte (Fig. 1a and b), (2) Li-metal mixed with spherical particles of Al$_2$O$_3$ (AOLi) combined with LPSC as solid electrolyte (Fig. 1c and d), (3) Li-metal mixed with spherical particles of BaTiO$_3$ (BTOLi) combined with LPSC as solid electrolyte (Fig. 1e and f) and (4) the same electrodes as (3) in combination with a composite electrolyte in which LPSC is also mixed with BTO (Fig. 1g–j).

As observed in Fig. 1a and **b** the electric field gradient is much larger near the tip of an inhomogeneity with a rectangular shape (1 μm × 2 μm) and a hemispherical tip (representing a Li-dendrite) at the Li-metal surface. Driven by the larger surface charge density present at the sharp electronically conducting feature, the electric field gradient increases dramatically at the tip of the Li-metal, which thus focuses the electric field lines to the tip of the Li-metal dendrite. This may facilitate Li-ion deposition at the tip of the dendrite representing the driving force for dendrite formation (independent of the thickness of the Li-metal electrode as can be confirmed by Figs. S1a and S1b). The electric field gradient around dendritic features at the surface penetrating into the solid electrolyte are unaffected and remain large upon the introduction of either BTO or AO to the electrode, Fig. 1c–f. This suggests that introducing the high dielectric material to the electrode alone may not be sufficient to suppress the growth of dendrites on the surface of the electrode.

When the Li-metal electrode is removed, leaving voids in the AO and BTO matrix, these dielectric fillers affect the electrical field gradients around dendritic features (Fig. S1c - **S1f**). In the case of the AO filler, the electric field gradient near the tip of the dendrite decreases slightly (Figs. S1c and d) in comparison with a dendrite in the solid electrolyte (Figs. S1a and b). Most interestingly, for the BTO filler, the electric field gradient at the tip of the dendrite disappears (Figs. S1e and f). The low polarizability of the AO makes the electric field gradient at the Li-metal tip remain, whereas the high polarizability of the BTO moves the electric
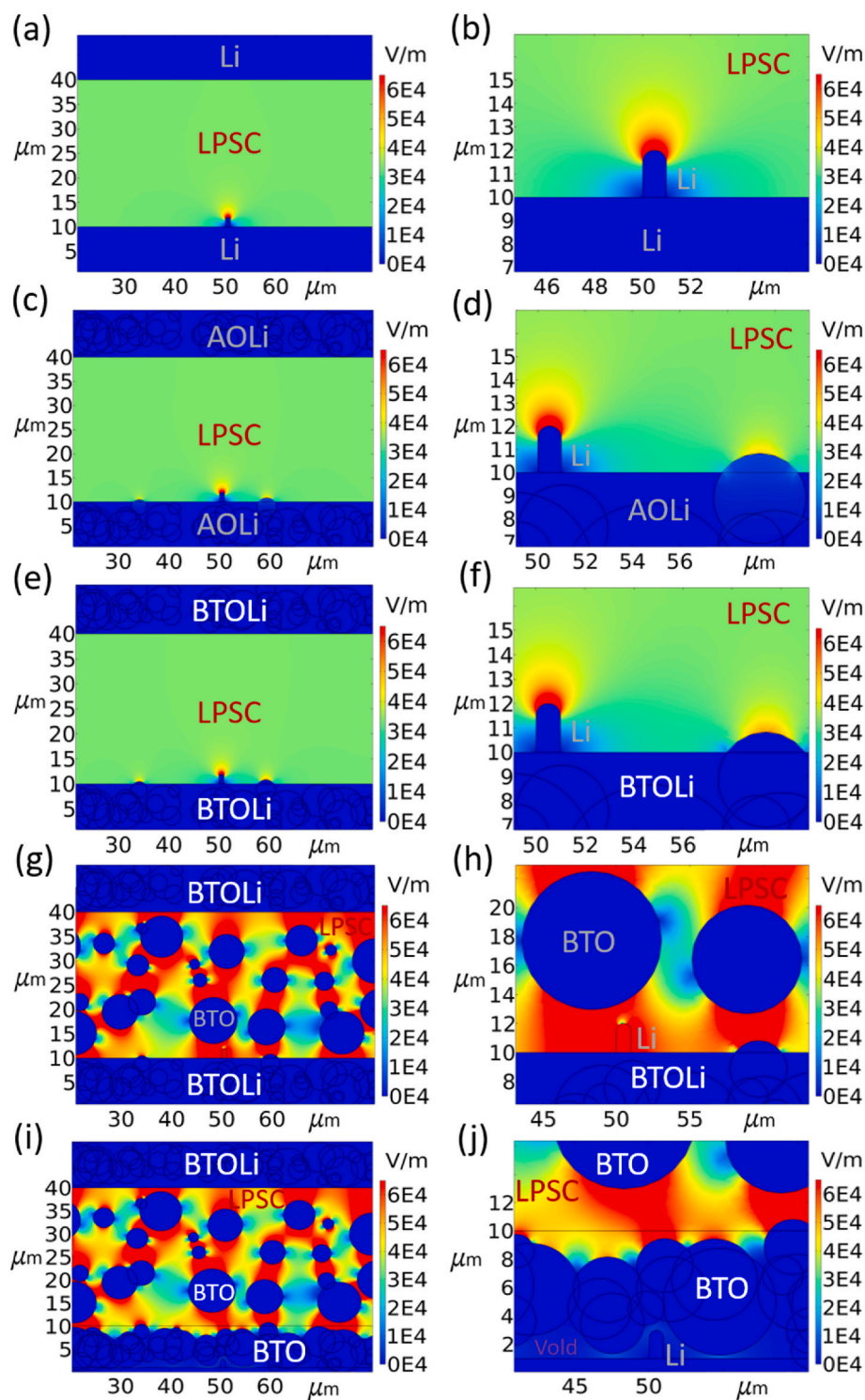
Fig. 1. Calculated electric field around Li metal inhomogeneities in 2D models having different configurations of symmetric lithium metal cells with different dielectric materials. Lithium dendrites are represented by a rectangular with a hemispherical tip. (a, b) Li/LPSC/Li cell, (c, d) AOLi/LPSC/AOLi cell, (e, f) BTOLi/LPSC/BTOLi cell, (g, h, i, j) BTOLi/LPSC and BTO mixture (BTOLPSC)/BTOLi cell. Units μm: micrometer, V: electric potential, V/m: electric field.

field lines away from the Li-metal tip towards the surface of the BTO itself. This suggests that the presence of high dielectric volumes in the vicinity of a Li-metal filament takes away the driving force for Li deposition at the tip of sharp features, thus taking away the driving force for tip-driven dendrite growth.

Fig. 1g and **h** represent the situation that a dendrite penetrates the solid electrolyte region and shows that high dielectric BTO has a distinct impact on the electric field gradients. As mentioned, the high electric field gradients are pulled towards the high dielectric, lowering the field gradient at the tip of dendritic features that penetrate the solid electrolyte (Fig. 1h). Based on this one could speculate that dendrites grow towards the BTO, whereby it poses a barrier for dendrites to continue their growth toward the counter electrode. Simultaneously, the electric field is also simulated in the stripped BTOLi/BTOLPSC cell configuration (Fig. 1i and **j**), where the electric field gradient at the tip of the dendrite has been taken away due to the presence of the high dielectric BTO

material, which may facilitate more compact Li-metal growth. Based on these simulations, the hypothesis is brought forward that a high dielectric 3D matrix, with lithium metal deposited in its voids, promotes homogeneous Li-metal growth, and that the high dielectric material added to the solid electrolyte may hinder dendrite growth through the solid electrolyte region. Fewer dendrites and more compact plating would lead to a contact area between Li-metal and the solid electrolyte interface, decreasing electrolyte decomposition due to reduction by Li-metal, promoting cycle life and lowering the chance of dendrites reaching the cathode that may lead to a short circuit.

2.2. Electrode preparation and morphology

In order to investigate the impact of high dielectric materials on the performance of Li-metal solid-state batteries, composite electrodes with either commercial AO (low dielectric constant) or BTO (high dielectric constant) were prepared and compared to establish the impact of the dielectric constant and differentiate from the impact of adding an inactive additive. Scanning electron microscopy (SEM) images (Fig. 2a and 2d) confirm that the micron-sized BTO and AO materials have similar particle sizes ranging from 1 up to 100 μm. The composite BTOLi and AOLi electrodes were prepared by melting lithium metal and mixing with BTO or AO powder in a Nickel crucible at 300 °C for 2 h, the details of which can be found in the methods section. The SEM images of Fig. 2b and e indicate that the molten lithium metal wets to the surface of the BTO and AO particles. Both the raw materials and composite electrolyte are characterized by X-ray diffraction (XRD) (Fig. S2), indicating that the bulk of the BTO is stable in contact with Li-metal, whereas the AO displays some reactivity, leading to the formation of a lithiophilic Li-Al-O interface [34]. The TiO_2 presented in the raw BTO was serving as a precursor for synthesizing the BTO material. Furthermore, Li_2TiO_3 is formed as a reaction product when Li metal reacts with TiO_2. During cycling, the Li_2TiO_3 phase undergoes de(lithiation), which will probably facilitate the process of lithium deposition. Both BTO and Li_2TiO_3 possess the ability to attract lithium ions towards themselves, rather than allowing them to accumulate at the tip of lithium dendrites. This characteristic proves beneficial for suppressing dendrite formation. However, given the relatively small amount of Li_2TiO_3 compared to the abundance of BTO particles, its presence is likely to have minimal impact on the behavior of lithium deposition. After pressing the as-prepared materials to a wafer layer under a mild pressure of 2 MPa, the 20% wt Li-metal, 80% wt BTO composite, BTOLi electrode (Fig. 2c), shows a relatively smooth surface as compared to the 20% wt Li-metal,

80% wt AO composite, AOLi electrode, Fig. 2f.

To determine the capacity of the prepared composite electrodes, the electrodes were assembled in a symmetric solid-state battery using LPSC as a solid electrolyte (see the Methods section for the preparation and XRD of the as-prepared material in Fig. S3) and Li-metal as the counter electrode. After stripping (electrochemical removal) Li completely from the BTOLi and AOLi composite electrodes at a current density of 0.1 mA cm^{-2}, a considerable specific capacity of 504 and 174 mA h g^{-1} was obtained (cutoff voltage 1 V vs Li/Li$^+$), respectively, where the specific capacities take into account both the weight of the AO/BTO matrix and the Li metal (Figs. S4a and b). For the BTOLi and AOLi composite electrodes (Figs. S4c and d), the smooth charging curve, without a second plateau, indicates that the total capacity is provided by metallic lithium only. In addition, the differential capacity curve further demonstrates that the redox reaction occurred around 0.02 V vs Li/Li$^+$ and thus represents lithium stripping. In this study, we have attempted to minimize the amount of additive material, to maximize the specific capacity. A higher specific capacity of 1260 mA h g^{-1} can be achieved by adjusting the Li/BTO ratio to 50% (Fig. S5). However, a specific capacity of 2000 mA h g^{-1} would require a volume percentage of 8% for the high dielectric BTO additive material [35].

To compare the surface morphologies of the bare Li anode with the composite AOLi and BTOLi anodes, SEM images were recorded after 10 cycles at a current density of 0.1 mA cm^{-2} towards a capacity of 0.5 mAh cm^{-2} (5 h), the results of which are shown in Fig. 3. (The SEM images of the LPSC solid electrolyte, and the LPSC and BTOLPSC pallets are shown in Fig. S6). SEM images of the pristine Li foil, AOLi, and BTOLi electrodes show that the Li foil and BTOLi electrodes have a relatively smooth surface, while some voids are observed for the AOLi electrode as compared to the BTOLi electrode, both prepared by the same pressure (Fig. 3a, d, g, j). After 10 cycles, the SEM image of the Li-metal anode, Fig. 3b, shows a micro-sized needle-like lithium dendrite on the surface of the lithium metal side, and on the electrolyte side (Fig. 3c) a micro-sized sharp electrodeposit penetrates the LPSC electrolyte. Also at the surface of the AOLi and BTOLi electrodes, Fig. 3e and h respectively, and on the side of the LPSC electrolyte, Fig. 3f and i respectively, large dendritic features and very rough surfaces are observed, demonstrating that dendrites can penetrate the solid electrolyte, preferentially growing through pores and cracks [36].

The situation substantially improves when BTO is added to both the anode and the LSPC electrolyte, in which case a more uniformly deposited Li-metal surface is observed. Fig. 3k and l show that the addition of BTO results in more uniformly deposited Li-metal and much
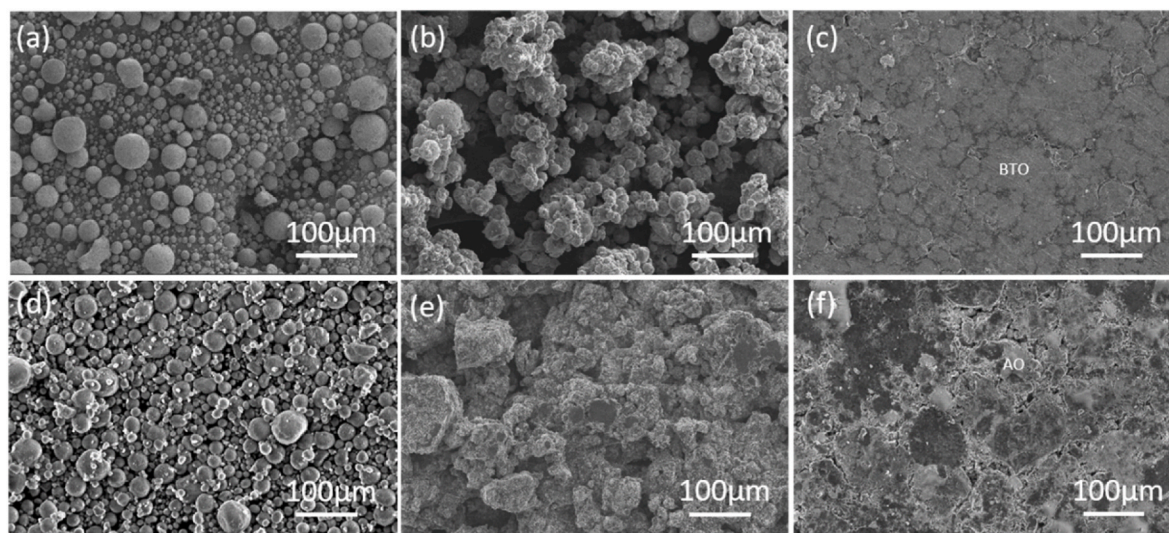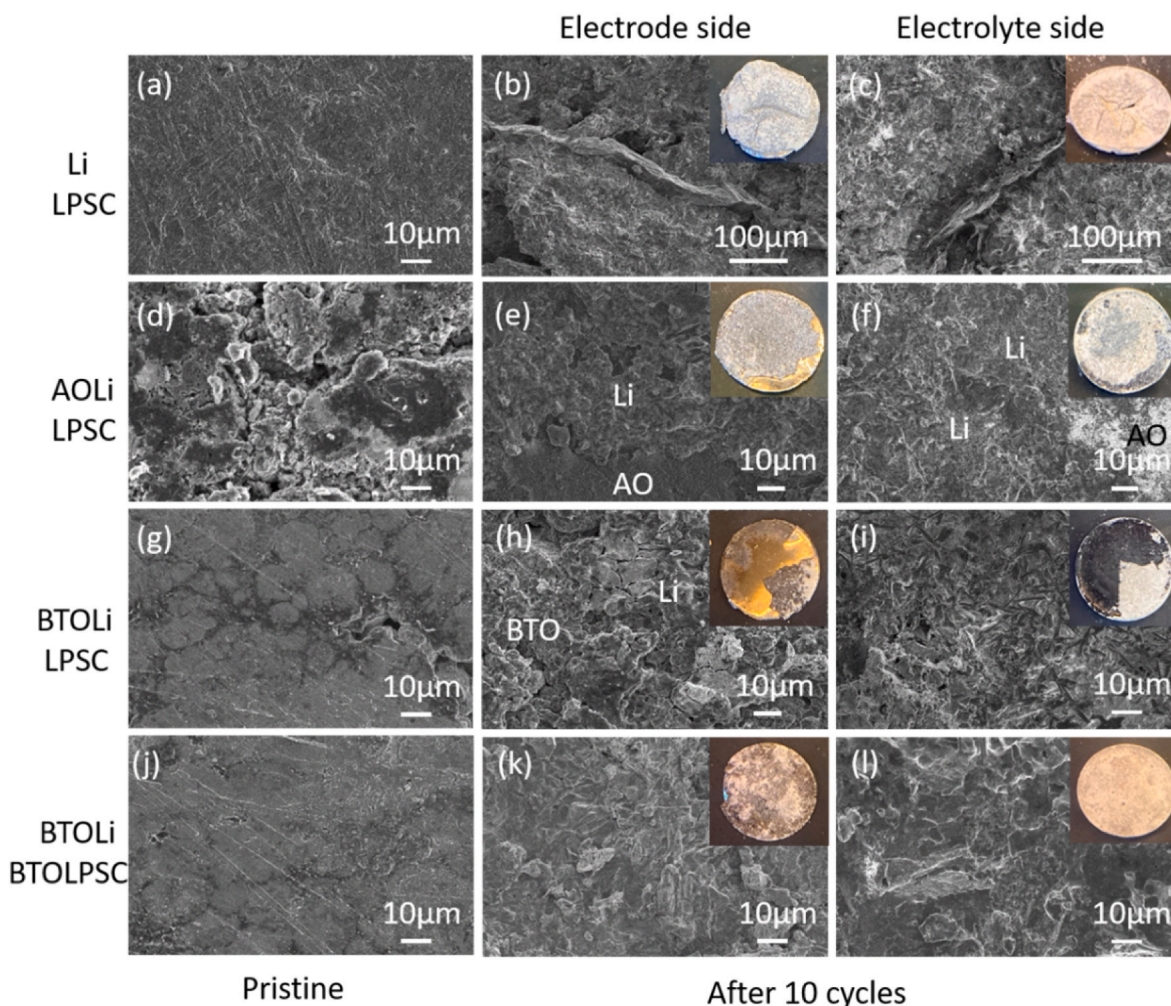

Fig. 2. Morphologies of pristine materials and as prepared composite Li-metal electrodes. (a–c) SEM images of pure BTO, 20%Li-BTO mixture, and the as-prepared BTOLi electrode, respectively. (d–f) SEM images of pure AO, 20%Li-AO mixture and the AOLi electrode, respectively.

Fig. 3. Morphologies of Li electrodeposits on the bare Li-metal electrode, AOLi, and BTOLi composite electrodes before and after 10 cycles at 0.1 mA cm^{-2} for 5 h. SEM images of the pristine surface of (a, d, g, j) Li-metal, AOLi, BTOLi, and BTOLI-BTOLPSC electrodes, respectively. SEM images of electrode side after cycling of (b, e, h, k) bare Li-metal, AOLi, BTOLi, and BTOLi-BTOLPSC cells, respectively. SEM images of the electrolyte side after cycling of (c, f, i, l) bare Li-metal, AOLi, BTOLi, and BTOLi-BTOLPSC cells, respectively. The insets show photographs of the electrodes.

less protrusion and pulverization on both the anode and the electrolyte, respectively. This supports the hypothesis that the addition of BTO leads to more homogeneous Li-metal deposition and additionally suggests that the BTO matrix may also suppress delamination. Both aspects are crucial to achieving stable Li-metal cycling in combination with solid electrolytes [15,37].

2.3. Electrochemical evaluation

2.3.1. Symmetrical cells

As a first step in evaluating the influence of the BTO and AO additives on the electrochemical performance, the critical current density at which dendrite formation is initiated is determined, by cycling symmetrical cells under an increasing current density. In Fig. 4, the results are shown for the Li/LPSC/Li, AOLi/LPSC/AOLi, BTOLi/LPSC/BTOLi, and BTOLi/BTOLPSC/BTOLi cells, cycled with current densities increasing from 0.1 mA cm^{-2} up to 1.0 mA cm^{-2}, followed by cycling at 0.1 mA cm^{-2} (detailed information can be found in Table S1). For the Li/LPSC/Li and AOLi/LPSC/AOLi cells, this results in a short circuit already after three cycles at 0.1 mA cm^{-2} (detailed voltage profiles are provided in Fig. S7). These short circuits are most likely due to dendrite formation, presumably supported by the relatively high electronic conductivity of LPSC (9.12×10^{-8} S cm^{-1}) [30,38,39]. The electric field calculations, shown in Fig. 1 and Fig. S1, suggest that the large electric

field gradient at Li-metal inhomogeneities is an important driving force for dendrite growth as commonly assumed [8,40]. The addition of the high dielectric material to the electrode in the BTOLi/LPSC/BTOLi cell results in a higher critical current density of 0.5 mA cm^{-2} with an average voltage hysteresis of 60 mV (Table S1 and Fig. S7). We propose that the higher critical current density is due to the presence of the high dielectric additives that lower the electric field gradient at the surface of the Li-metal (Figs. S1e and f), and not due to the presence of the additive itself because the low dielectric AO additive does not improve the critical current.

Although adding BTO can thus increase the critical current, dendrite formation may still be initiated by the high electric field gradient in the solid electrolyte region when the plating has filled the BTO matrix (see the simulations of Fig. 1 g, h). To hinder this, BTO is also added to the electrolyte. As a first step that helps us in choosing the amount of BTO that we add to the electrolyte, we determine the impact of the BTO fraction on the conductivity of the solid electrolyte composite with electrochemical impedance spectroscopy (EIS). Fig. S8 presents the results for different weight ratios between BTO and LPSC. The resulting ionic conductivities of pure LPSC electrolyte, 15% wt BTO with 85 %wt LPSC (15%BTO-LPSC) and 30% wt BTO with 70% wt LPSC (30%BTO-LPSC) mixtures are 5.6, 4.5 and 0.73 mS cm^{-1}, respectively. As the ionic conductivity of the 30%BTO-LPSC mixture is significantly smaller, the 15%BTO-LPSC composite is used as an electrolyte for further
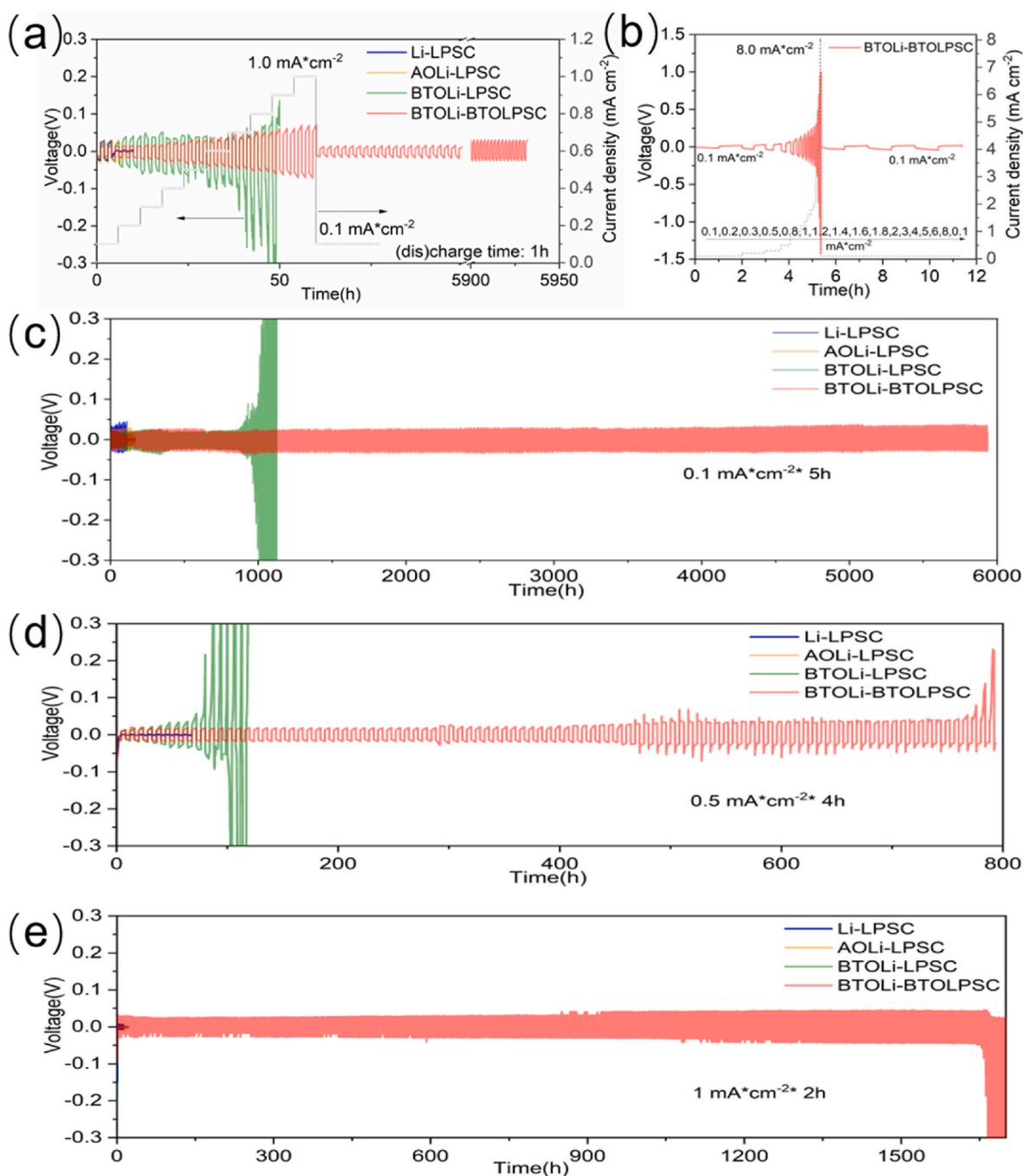
Fig. 4. Critical current density and cycling test of symmetric cells using bare Li electrodes, AOLi or BTOLi composite electrodes, and LPSC or BTOLPSC electrolytes. (a) Voltage profile at an increasing current density from 0.1 mA cm^{-2} to 1.0 mA cm^{-2} followed by 0.1 mA cm^{-2} cycling ((dis)charge time was 1h). (b) Voltage profiles of the symmetric cell using BTOLi composite electrode and BTOLPSC electrolyte cycled under the current density of 0.1 mA cm^{-2} to 8.0 mA cm^{-2} with a fixed capacity of 0.1 mA h cm^{-2}. Voltage profiles of cycling performance at a current density of (c) 0.1 mA cm^{-2} with a capacity of 0.5 mA h cm^{-2}, (d) 0.5 mA cm^{-2} with a capacity of 2.0 mA h cm^{-2}, (e) 1 mA cm^{-2} with a capacity of 2.0 mA h cm^{-2}, respectively.

experimental evaluation.

The electrochemical results of the BTOLi/BTOLPSC/BTOLi cell that contains 15%BTO-LPSC as an electrolyte can resist the highest current density among all cells, and thus even higher than the cell with only BTO added to the electrodes. The cell can easily handle a current density of 1.0 mA cm^{-2} with a potential hysteresis of just 65 mV as shown in Fig. 4a and Table S1. Subsequently, cycling at 0.1 mA cm^{-2} can be maintained for at least 6000 h with a very low overpotential of 21 mV after 6000 h. The much better rate capability of the cell with BTO added to both the electrode and electrolyte suggests that dendrite formation and growth

are suppressed. This is in line with the electric field calculations that demonstrate that the presence of the high dielectric BTO additive removes the electric field gradients at inhomogeneous Li-metal features, both in the anode and in the solid electrolyte region. In addition, the improved performance may in part be ascribed to the lower electronic conductivity of the 15% BTO-LPSC solid electrolytes (1.14×10^{-8} S cm^{-1}) as compared to that of the pure LSPC electrolyte (9.12×10^{-8} S cm^{-1}), values that were determined through direct current polarization method. Han et al. indicated that a higher electronic conductivity of the solid electrolytes promotes dendrite formation [36] while on the other

hand, a high Li-ion conductivity suppresses dendrite formation. Oppositely, as the ionic conductivity of LSPC (5.6 mS cm^{-1}) is slightly higher than the BTOLSPC composite (4.5 mS cm^{-1}) adding BTO can also be argued to promote dendrite formation. Meanwhile, the stable and smooth cycling result of Li/BTOLPSC/Li cell (Fig. S9) verified our hypothesis that dendrites can be suppressed with BTO particles added into the LPSC electrolyte, thus the BTOLPSC composite. As there are multiple factors at play, it is not possible to disentangle the impact of decreasing the ionic conductivity and increasing the electronic conductivity at the same time. However, the electric field gradient calculations suggest that the BTO in the solid electrolyte region suppresses the driving force for dendrite formation, providing a rationale for the larger critical current and more stable cycling observed in Fig. 4.

To further examine the limits of the BTOLi composite in combination with the BTOLPSC electrolyte, a symmetric Li-metal cell was cycled to higher current densities. The measurements, displayed in Fig. 4b and Fig. S10 and performed with current densities of 0.1 mA cm^{-2} up to 8.0 mA cm^{-2} under a fixed capacity of 0.1 mA h cm^{-2} and limited by a 1.0 V vs Li/Li$^+$ stripping cut-off voltage, demonstrate that this solid-state battery can prevent a short circuit and has low overpotentials even at these high current densities. Under all conditions, the BTOLi/BTOLPSC/BTOLi cell outperforms the other cell configurations and has a higher current density, larger cycling capacity (tested up to 2 mA h cm^{-2}), and cycling duration (Fig. 4c–e and Figs. S11–13). In fact, the areal capacity of 2 mA h cm^{-2} is among the highest reported in the open literature for solid-state Li metal batteries (see Table S2). The over-potentials of only 11, 36, and 48 mV under current densities of 0.1, 0.5, and 1.0 mA cm^{-2} indicate less formation of poorly conducting decomposition products, also suggesting more uniform Li-metal plating and stripping as a consequence of introducing the high dielectric BTO. Furthermore, the BTOLi/BTOLPSC/LTO cell configuration stands out by displaying much lower polarization during cycling, reflecting a much more stable anode-

solid electrolyte interface, that is responsible for the relatively long cycle life.

2.3.2. Full cell cycling when paired with a Li$_4$Ti$_5$O$_{12}$ cathode

We further illustrate the performance of the BTOLi anode by pairing it with Li$_4$Ti$_5$O$_{12}$ (LTO) as the cathode, approaching a more realistic configuration. LTO was selected because of its extremely small volumetric change upon (de)lithiation and a working potential (1.55 V vs Li/Li$^+$) within the electrochemical stability window of LPSC [21,22,41]. Thereby, the degradation of the cell will be mainly due to the Li-metal anode, which allows us to evaluate the impact of the dielectric constant of the solid additives. Fig. 5 shows the capacity upon galvanostatic cycling at a current density of 0.32 mA cm^{-2} for the four battery configurations when paired with the Li$_4$Ti$_5$O$_{12}$ cathode. The mass loading for the LTO, having a theoretical specific capacity of 175 mA h g^{-1}, is approximately 6.0 mg cm^{-2}. Fig. 5a and **b** show rapid capacity fading for both the Li-metal and AOLi anodes having an average Coulombic efficiency of 131.9% and 122.8% respectively, signifying the large reactivity of the LPSC electrolyte that increases the charge capacity [8,30,42]. Although the BTOLi/LPSC/LTO cell (Fig. 5c) also shows rapid capacity fading upon cycling, it is less severe due to the improved Coulombic efficiency (average 108.9%), demonstrating that BTO in the Li-metal anode improves the reversibility. The comparison to the AO additive suggests that this improvement is the consequence of the high dielectric constant. A major improvement is observed when BTO is also added to the LPSC solid electrolyte, where the BTOLi/BTOLPSC/LTO cell results in an average Coulombic efficiency of 100.4% in combination with much less solid electrolyte decomposition. For this cell, the capacity is maintained for 90% over 500 cycles as observed in Fig. 5d. The rate performance of both Li/LPSC/LTO cells and BTO-Li/BTOLPSC/LTO cells was tested at various current densities ranging from 0.16 mA cm^{-2} to 1.28 mA cm^{-2}, as shown in Fig. S14. The

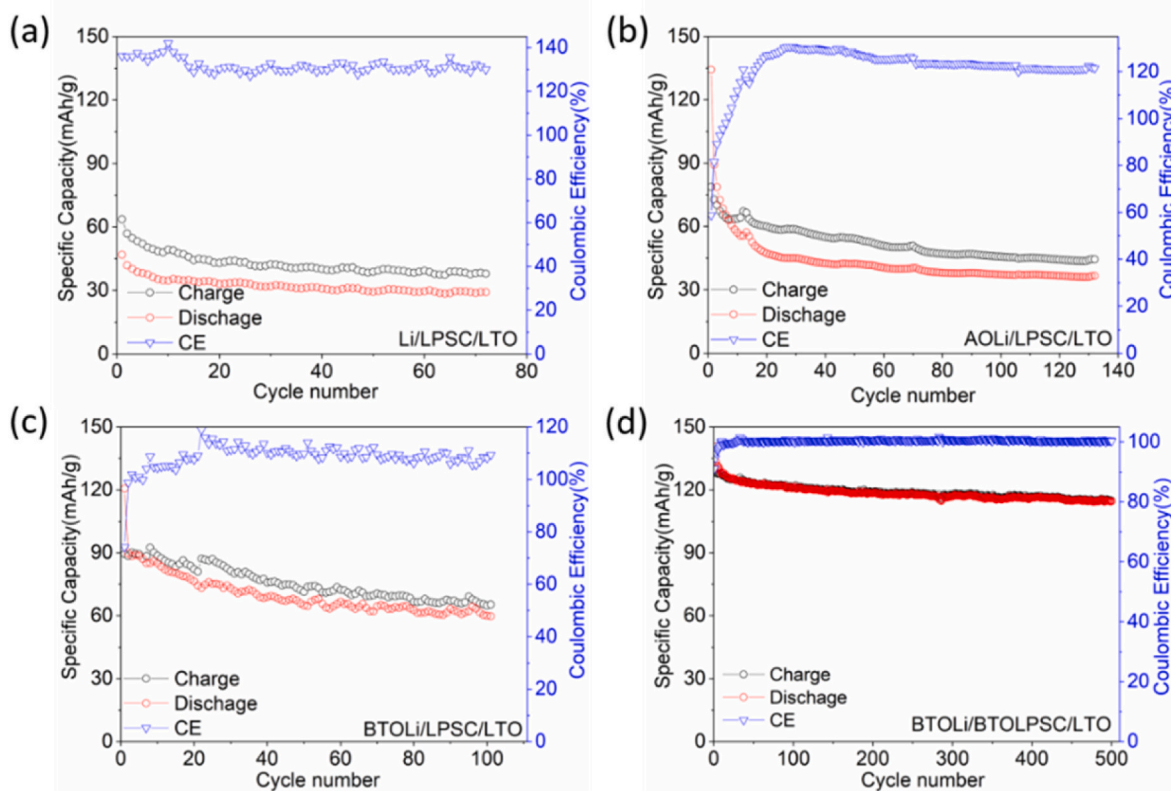**Fig. 5.** Electrochemical cycling performance at 0.32 mA cm^{-2} the Li-metal, AOLi, BTOLi anodes with a Li$_4$Ti$_5$O$_{12}$ cathode in combination with the LPSC and BTOLPSC solid electrolytes. Cycling performance of (a) the Li/LPSC/LTO cell, (b) the AOLi/LPSC/LTO cell, (c) the BTOLi/LPSC/LTO cell, and (d) the BTOLi/BTOLPSC/LTO cell.

BTOLi/BTOLPSC/LTO cell, incorporating the BTO filler, exhibits an average Coulombic efficiency of 99.98%, indicating a more stable interface compared to the Li/LPSC/LTO cell, which has an average Coulombic efficiency of 129.27%. Evaluation of the voltage curves during these cycling experiments, shown in Fig. S15, indicates high overpotentials for the Li/LPSC/LTO, AOLi/LPSC/LTO and BTO-Li/LPSC/LTO cells (Table S3). This reflects a high internal resistance, which can be ascribed to the formation of poorly conducting decomposition products and contact loss at the interface between the anode and solid electrolyte (see also the EIS and XPS results) [8,17,33]. The BTOLi/BTOLPSC/LTO cell stands out by displaying much lower polarization during cycling, reflecting a much more stable anode-solid electrolyte interface, that is responsible for the relatively long cycle life.

2.4. Interfacial analysis and decomposition suppression

2.4.1. Electrochemical impedance spectroscopy

To study the effect of the BTO additives on the interfacial resistance, Electrochemical impedance spectroscopy (EIS) measurements are performed after cycling at 0.1 mA cm^{-2} to 0.5 mA h cm^{-2}. These measurements are shown in Fig. 6 while additional results are provided in Table S4. The quarter-circle and semicircle obtained in the high-frequency range (100 kHz - 10 Hz) can be ascribed to the SEI and charge-transfer resistance [30,34]. Already before cycling, the spontaneous (electro)chemical reaction of Li-metal with LPSC may result in less conductive decomposition products (Li$_2$S, LiCl, and Li$_3$P) [8,40,43], which are held responsible for the relatively high interfacial resistance of ≈159 Ω. The three other configurations lead to a slightly smaller but comparable interface resistance (see Table S4). As expected, after

cycling the interfacial resistance of both the Li/LPSC and AOLi/LPSC interfaces increase significantly by about 20% after 10 cycles, which is known to be the consequence of further decomposition reactions amplified by Li-dendritic growth and contact loss [8,30,44].

The presence of BTO, especially when added to both the Li-metal and LPSC solid electrolyte, suppresses the rise in interface resistance upon cycling. Indeed, the resistance barely changes upon cycling for the BTOLi-BTOLPSC cell and equals 95, 93, and 99 Ω after 1, 10, and 100 cycles, respectively (see Table S4). This can be rationalized by the suppression of dendrites, leading to less LPSC decomposition products, and thus a better ability to maintain a low interface resistance, in agreement with the smaller overpotential during cycling and more stable cycling observed in Fig. 4.

2.4.2. X-ray photoelectron spectroscopy

XPS measurements are performed to study if the addition of BTO to the electrolyte suppresses the formation of decomposition products at the electrode-solid electrolyte interface upon cycling, as suggested by the more reversible cycling observed. To facilitate these measurements, cells were disassembled after cycling and the interface was isolated by carefully scraping it from the electrode (see methods and materials). The XPS results, displayed in Fig. 7, show for all samples strong doublet peaks at binding energies of $BE \approx 131.8$ eV (P2p scan), $BE \approx 161.5$ eV (S2p scan), $BE \approx 198.5$ eV (Cl2p scan), and a single peak at $BE \approx 55$ eV (Li1s scan), previously identified as peaks that belong to LPSC [45–47]. In addition, in all samples additional peaks are observed at $BE \approx 133.5$ eV (P2p scan) and $BE \approx 160.5$ eV (S2p scan), being the signatures of Li$_3$PO$_4$ (or P$_2$S$_x$) and Li$_2$S, respectively [45–48]. We attribute the presence of the majority of these phases, previously observed in pristine
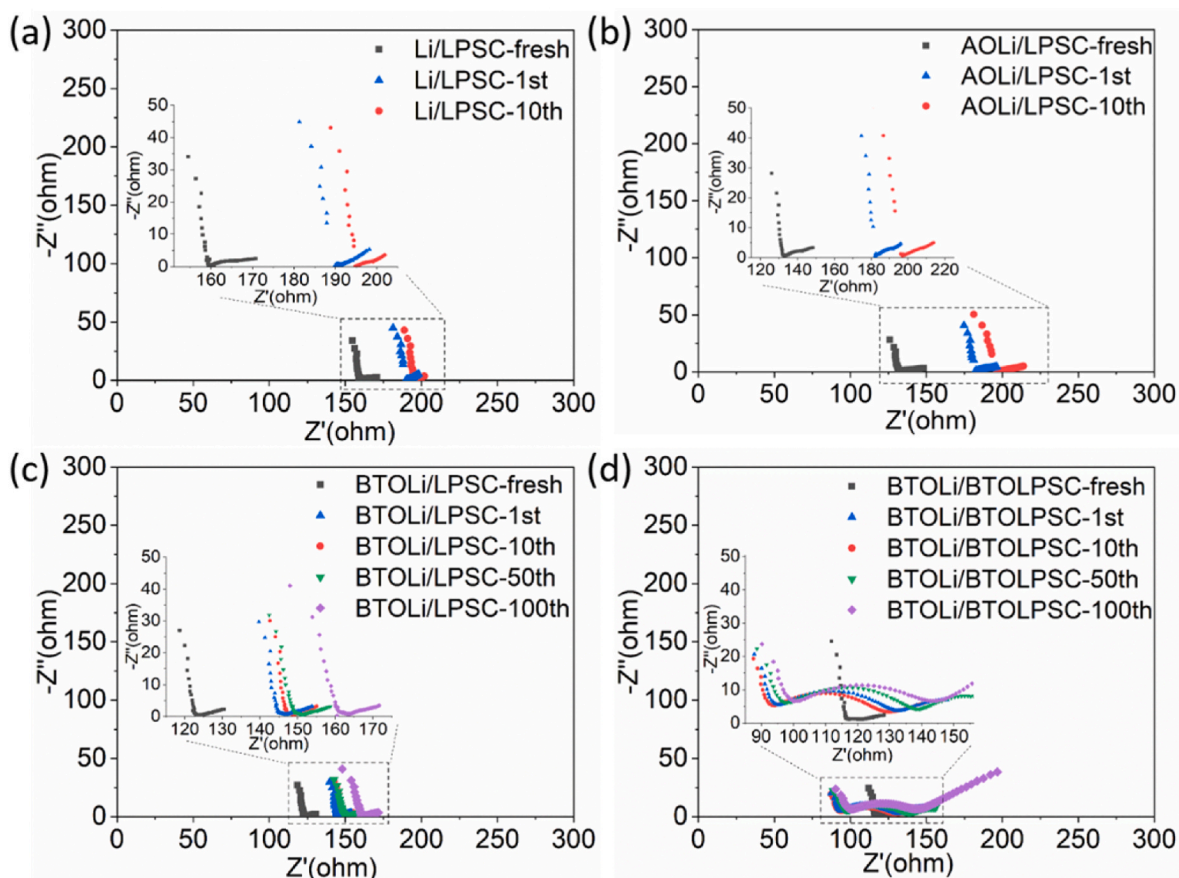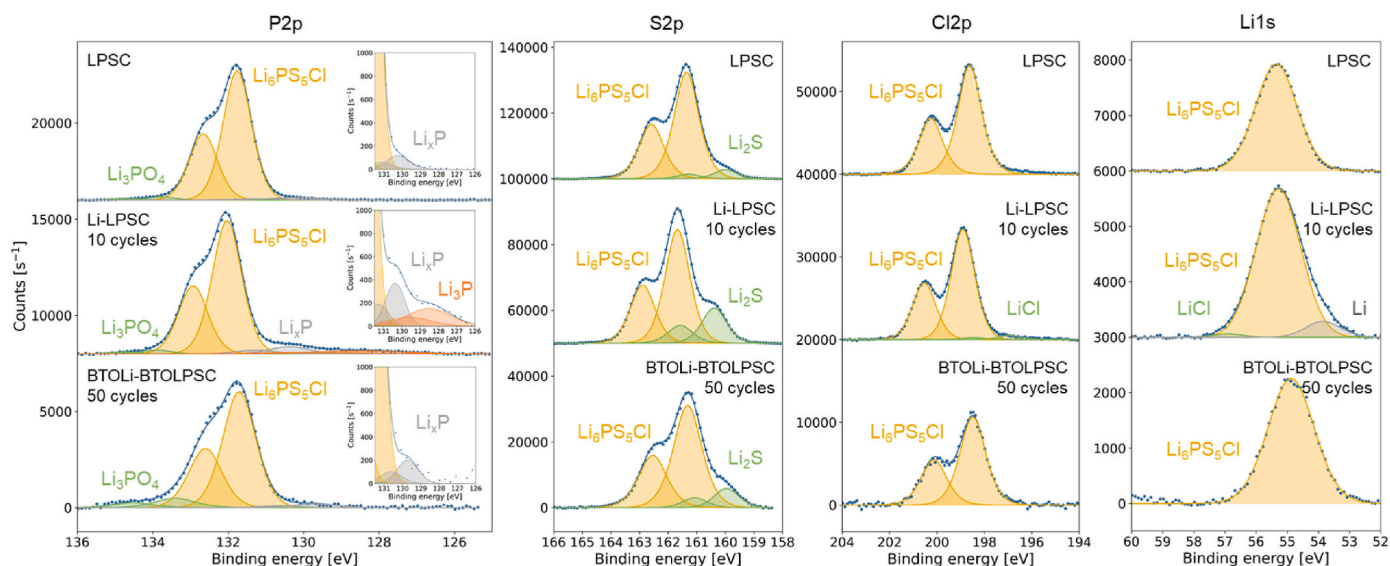

Fig. 6. Electrochemical impedance spectroscopy (EIS) results displayed as Nyquist plots of the solid-state symmetric cells after different numbers of cycling at 0.1 mA cm^{-2} for 5 h. (a) Li-metal with LPSC (Li-LPSC), (b) Li-metal-AO composite with LPSC (AOLi-LPSC), (c) Li-metal-BTO composite with LPSC (BTOLi-LPSC) (d) Li-metal-BTO composite with the LPSC-BTO composite (BTOLi-BTOLPSC).

Fig. 7. XPS spectra of pristine LPSC and LPSC after cycling in a Li-LPSC-Li cell for 10 cycles and 50 cycles in a BTOLi-BTOLPSC-BTOLi cell. To aid the comparison, the counts of the BTOLi-BTOLPSC have been multiplied by a factor of 4. The lower count rate for this sample is attributed to (i) the lower percentage of LPSC in the sample and (ii) a smaller coverage of the carbon tape by the samples studied.

LPSC electrodes [45], to impurities in the raw materials and/or traces of reagents used for the synthesis of the electrolyte and to spontaneous (electro)chemical reaction of Li-metal with LPSC.

Most importantly, the XPS measurements indicate that the addition of BTO suppresses the formation of some critical non-conductive decomposition products. While Li_3P is identified in the cycled Li-LPSC-Li cell, Li_3P is not detected in the cycled BTOLi-BTOLPSC-BTOLi cell. The Li_3P peak [49–51], observed in the P2p scan at $BE \approx 128$ eV in the Li-LPSC-Li sample, is relatively small, yet its presence is significant. In addition, LiCl is formed, as evidenced by the peaks at $BE \approx 196.5$ eV and $BE \approx 56.2$ eV in the Cl2p and Li1s scan, respectively [45,46,52]. For the BTOLi-BTOLPSC-BTOLi sample, no Li_3P has been identified while the Li_xP peak is significantly smaller as compared to the Li-LPSC-Li sample. We have repeated this measurement 13 times on samples cycled 10, 30, and 50 cycles. In none of these measurements, Li_3P was observed while the Li_xP peak was in all cases significantly smaller compared to that observed for the Li-LPSC-Li samples, and these measurements indicate that BTO is effective in suppressing the formation of reduced phosphorus species like Li_xP and especially Li_3P. Furthermore, solid-state ^{31}P NMR results reported in Fig. S16 show that the formation of Li_3PS_4 is suppressed by the addition of BTO to the LSPC electrolyte.

In summary, the XPS and NMR measurements indicate that the addition of BTO suppresses the formation of decomposition products, explaining the lower interfacial resistance observed by EIS (Fig. 6 and Table S4). It also suggests the suppression of dendrites as these can be expected to amplify the formation of decomposition products [8,30,44]. On the macroscopic, this is in accordance with the smaller overpotential during cycling and longer capacity retention and cell life observed in Fig. 4.

3. Conclusion

To conclude, the addition of BTO, a high dielectric material, to the Li-electrode and the LSPC solid electrolyte appears to be an effective method to suppress Li metal filament and dendrite formation. In comparison with a low dielectric additive and the absence of an additive, the BTO results in a significantly higher critical current density, more stable cycling performance of the solid-state Li metal symmetrical cell, and the BTOLi/BTOLPSC/LTO full cell configuration (500 cycles, 90% capacity retention), a much lower impedance upon cycling in a symmetrical cell geometry and in a significant reduction of the LPSC decomposition

products as observed by XPS and solid-state ^{31}P NMR. Electric field calculations indicate that BTO suppresses dendrite formation through lowering the electric field gradients at the Li metal anode surface. In addition, when BTO is added to the solid electrolyte matrix it lowers the overall electronic conductivity which may contribute to the suppression of dendrite penetration although this effect may be in part compensated by the lower ionic conductivity of the solid electrolyte matrix. High dielectric additives are thus suggested as an effective strategy to suppress dendrite growth and solid electrolyte decomposition in solid-state batteries.

4. Experimental

4.1. Preparation of anode materials and solid-state electrolytes

Commercial $BaTiO_3$ (Sigma-Aldrich, denoted as BTO) and Al_2O_3 (Sigma-Aldrich, denoted as AO) powder were used as the starting materials, because of their different dielectric constants. Firstly, metallic lithium (20% wt) was heated in a nickel crucible at 300 °C for 0.5 h, and subsequently, BTO or AO (80% wt) powder was added and mixed with the molten lithium metal. After 2 h of mixing and heating, the prepared materials (BTOLi or AOLi composites) were collected. The solid-state electrolyte Li_6PS_5Cl (denoted as LPSC) was prepared by a simple solid-state reaction. The stoichiometric raw materials LiCl (Sigma-Aldrich), P_2S_5 (Sigma-Aldrich), and Li_2S (Sigma-Aldrich) were used as the starting materials and were ball milled at 110 rpm for 2 h in ZrO_2 coated jars using 18 ZrO_2 balls. After ball milling, the precursor was sealed in a quartz tube with Ar and then annealed at 550 °C for 15 h to obtain the LPSC solid electrolyte. Commercial $Li_4Ti_5O_{12}$ (denoted as LTO) was chosen as the cathode material to assemble cells. LTO, LPSC and carbon black were ball milled in a mass ratio of 4:4:2 at 200 rpm for 6 h to prepare the cathode mixture.

4.2. Characterization of the materials and the electrodes

X-ray Diffraction (XRD) was performed both on the powder and pallets to identify the crystalline phases of the prepared materials by measuring with a 2θ range of 10 - 80° using $Cu_{K\alpha}$ X-rays (1.5406 Å at 45 kV and 40 mA) on an X'Pert Pro X-ray diffractometer (PANalytical). To prevent reaction with air, the samples were sealed in an airtight homemade XRD sample holder with a capton window in an Argon-filled

glove box. Ionic conductivities of the LPSC solid electrolyte and the BTOLPSC mixture were measured by making pallets having a diameter of 10 mm. Stainless-steel current collectors were attached to both sides of the wafers and alternating current impedance measurements were conducted on an Autolab (Autolab PGSTAT302 N) in the frequency range of 0.1 Hz–100 kHz with a perturbation potential of 5 mV. Electronic conductivities of the LPSC solid electrolyte and BTOLPSC mixture were measured using the Direct Current Polarization method. A one-side blocking cell (like Li-In/LPSC/Stainless steel) was assembled and tested with the Autolab. Lithium metal plating wafer electrodes for SEM tests were prepared by (dis)charging the solid-state cells for several cycles. Before the scanning electron microscope (SEM) imaging, the wafer electrodes were pressed out from the Al_2O_3 ceramic cylinder in the glove box. Subsequently, the samples were transferred into a SEM (JEOL JSM-6010LA) machine under dry Argon condition, and images were taken using an accelerating voltage of 2–10 kV.

4.3. Solid-state NMR

Solid-state NMR measurements were performed using a Bruker Ascend 500 MHz spectrometer equipped with two-channel 4.0 mm MAS probes. The operating frequency for ^{31}P was 202.47 MHz, and all measurements were performed within a spinning speed range of 8 kHz and $\pi/2$ pulse lengths of 4 µs were determined for ^{31}P. The chemical shifts of ^{31}P spectra were referenced with respect to 85% H_3PO_4 solution. Based on the spin-lattice (T_1) relaxation time, recycle delays of 20 s were used, collecting 1024 scans.

4.4. X-ray photoelectron spectroscopy (XPS)

XPS measurements were performed with a ThermoFisher K-Alpha spectrometer to investigate the chemical state of the elements present. The spectrometer is equipped with a focused monochromatic Al kα source (1486.6eV) anode operating at 36W (12 kV, 3 mA), a flood gun operating at 1V, 100 µA, and the base pressure in the analysis chamber is approximately 2×10^{-9} mbar. The spot size is approximately 800×400 µm^2 and the pressure in the analysis chamber is about 2×10^{-9} mbar. The pass energy of the analyzer was set to 50 eV. A thin layer of the powder sample, carefully isolated from the electrode-solid electrolyte interface, was deposited on a substrate consisting of copper foil and carbon tape inside an argon-filled glove box. These samples were transported in a vacuum transfer module to the XPS without exposure to air. The binding energy was corrected for the charge shift by taking the primary C1s hydrocarbon peak at $BE = 284.8$ eV as a reference. This resulted in a correction of the BE of at max 0.4 eV. The XPS spectra were fitted using a pseudo-Voigt with a 70% Gaussian and a 30% Lorentzian contribution (weighted least-squares fitting method) and a nonlinear Shirley-type background.

4.5. Assembly and electrochemical tests of the cells

Symmetric solid-state cells (AOLi/LPSC/AOLi, BTOLi/LPSC/BTOLi, BTOLi/BTOLPSC/BTOLi, and Li/LPSC/Li) were assembled in an argon-filled glove box in the following steps: 200 mg of LPSC or BTOLPSC was pressed tightly under the pressure of 300 MPa as the electrolyte layer, and then 10 mg of BTOLi or AOLi (or Li metal disk with a diameter of 7 mm, 0.5 mm thickness) was added to both sides of the electrolyte layer, separately. After that, 2 MPa pressure was used to press these three layers together. The (dis)charge processes of these symmetric cells were performed on a Maccor battery tester (Model 4300) in the glovebox at room temperature. The cells were cycled in the potential range of $-4.0 – 1.0$ V (vs. Li/Li$^+$) with the current densities from 0.1 mA cm^{-2} to 8 mA cm^{-2}. The electrochemical impedance spectroscopy (EIS) of cells was measured before and after cycling on an Autolab (Autolab PGSTAT302 N) in the frequency range of 0.1 Hz–100 kHz. A perturbation of 5 mV was applied. The Li/LPSC/LTO and BTOLi/BTOLPSC/LTO half cells

were assembled in the same way and were cycled within the potential range of 1.0–2.5 V (vs. Li/Li$^+$) at 0.32 mA cm^{-2} at room temperature in the glove box.

4.6. Electric field calculations

The simulations were performed in COMSOL Multiphysics 5.5 in which a basic 2D voltaic cell was constructed to represent a solid-state electrolyte cell. Using the electrostatics software, the electric field throughout the cell was calculated. Several materials were defined by their dielectric constant. As a standard, the electrodes used were lithium which was taken from the COMSOL materials library. This work looks at four different types of cells, each with different electrodes and electrolytes. Electrodes of lithium metal, Li-BaTiO$_3$ (BTOLi), or Li-Al$_2$O$_3$ (AOLi) (10 µm × 100 µm) were placed at two sides of the solid electrolyte Li$_6$PS$_5$Cl (LPSC) or Li$_6$PS$_5$Cl and BaTiO$_3$ mixture (BTOLPSC) (30 µm × 100 µm) to approximate the situation of the real battery. A lithium dendrite, represented by a rectangular shape (1 µm × 2 µm) with a hemispherical tip, is placed on the top of the electrode. High dielectric materials (BTO and AO), modeled as round particles with a size between 1 and 8 µm, were randomly added to the electrodes. The relative permittivities of BTO, AO, and the LPSC electrolyte are 4000, 8, and 5, respectively. There are several limitations of these static simulations. In the first place, it does not take into account modulation of the local electrical field due to the double layer of the dendrite and the current density under operation conditions, which in general will increase the electrical field gradient at the dendrite. Dynamic simulations of dendrite growth at relatively large overpotentials (0.45 V) however indicate that this is responsible for a small contribution (~1%) compared to the electrical field gradient under static conditions [53]. Another aspect is the strain in the BTO due to a local electrical field, the piezoelectric effect. However, considering that the simulated electrical field gradients do not exceed 10^5 V/m, the strain is anticipated to be well below 1% [54], which we assume has no impact on the system.

CRediT authorship contribution statement

Chao Wang: Conceptualization, Methodology, Investigation, Data curation, Writing – original draft, Writing – review & editing. **Ming Liu:** Investigation, Data curation, Writing – review & editing. **Lars J. Bannenberg:** Data curation, Writing – review & editing. **Chenglong Zhao:** Investigation, Data curation. **Michel Thijs:** Investigation, Data curation. **Bart Boshuizen:** Investigation. **Swapna Ganapathy:** Investigation, Data curation. **Marnix Wagemaker:** Conceptualization, Supervision, Writing – original draft, Writing – review & editing.

Declaration of competing interest

The authors declare that they have no known competing financial interests or personal relationships that could have appeared to influence the work reported in this paper.

Data availability

Data will be made available on request.

Acknowledgments

Appendix A. Supplementary data

Supplementary data to this article can be found online at https://doi.org/10.1016/j.jpowsour.2023.233768.

References

[1] J.B. Goodenough, K.-S. Park, J. Am. Chem. Soc. 135 (2013) 1167–1176.
[2] J.B. Goodenough, Y. Kim, Chem. Mater. 22 (2010) 587–603.
[3] B. Dunn, H. Kamath, J.-M. Tarascon, Science 334 (2011) 928–935.
[4] M. Armand, J.-M. Tarascon, Nature 451 (2008) 652–657.
[5] J.-M. Tarascon, M. Armand, Materials for Sustainable Energy: a Collection of Peer-Reviewed Research Review Articles from, Nature Publishing Group, 2011, pp. 171–179.
[6] P.G. Bruce, S.A. Freunberger, L.J. Hardwick, J.-M. Tarascon, Nat. Mater. 11 (2012) 19–29.
[7] J. Janek, W.G. Zeier, Nat. Energy 1 (2016), 16141.
[8] K.B. Hatzell, X.C. Chen, C.L. Cobb, N.P. Dasgupta, M.B. Dixit, L.E. Marbella, M.T. McDowell, P.P. Mukherjee, A. Verma, V. Viswanathan, ACS Energy Lett. 5 (2020) 922–934.
[9] T. Famprikis, P. Canepa, J.A. Dawson, M.S. Islam, C. Masquelier, Nat. Mater. 18 (2019) 1278–1291.
[10] K. Xu, Chem. Rev. 114 (2014) 11503–11618.
[11] A. Manthiram, X. Yu, S. Wang, Nat. Rev. Mater. 2 (2017).
[12] K. Fu, Y. Gong, G.T. Hitz, D.W. McOwen, Y. Li, S. Xu, Y. Wen, L. Zhang, C. Wang, G. Pastel, J. Dai, B. Liu, H. Xie, Y. Yao, E.D. Wachsman, L. Hu, Energy Environ. Sci. 10 (2017) 1568–1575.
[13] F. Shen, M.B. Dixit, X. Xiao, K.B. Hatzell, ACS Energy Lett. 3 (2018) 1056–1061.
[14] J. Tippens, J.C. Miers, A. Afshar, J.A. Lewis, F.J.Q. Cortes, H. Qiao, T.S. Marchese, C.V. Di Leo, C. Saldana, M.T. McDowell, ACS Energy Lett. 4 (2019) 1475–1483.
[15] M. Nagao, A. Hayashi, M. Tatsumisago, T. Kanetsuku, T. Tsuda, S. Kuwabata, Phys. Chem. Chem. Phys. 15 (2013) 18600–18606.
[16] L. Porz, T. Swamy, B.W. Sheldon, D. Rettenwander, T. Frömling, H.L. Thaman, S. Berendts, R. Uecker, W.C. Carter, Y.-M. Chiang, Adv. Energy Mater. 7 (2017).
[17] P. Albertus, S. Babinec, S. Litzelman, A. Newman, Nat. Energy 3 (2018) 16–21.
[18] N. Kamaya, K. Homma, Y. Yamakawa, M. Hirayama, R. Kanno, M. Yonemura, T. Kamiyama, Y. Kato, S. Hama, K. Kawamoto, Nat. Mater. 10 (2011) 682–686.
[19] L.E. Marbella, S. Zekoll, J. Kasemchainan, S.P. Emge, P.G. Bruce, C.P. Grey, Chem. Mater. 31 (2019) 2762–2769.
[20] M. Liu, C. Wang, Z. Cheng, S. Ganapathy, L.A. Haverkate, S. Unnikrishnan, M. Wagemaker, ACS Mater. Lett. 2 (2020) 665–670.
[21] T.K. Schwietert, V.A. Arszelewska, C. Wang, C. Yu, A. Vasileiadis, N.J. de Klerk, J. Hageman, T. Hupfer, I. Kerkamm, Y. Xu, E. van der Maas, E.M. Kelder, S. Ganapathy, M. Wagemaker, Nat. Mater. 19 (2020) 428–435.
[22] Y. Zhu, X. He, Y. Mo, ACS Appl. Mater. Interfaces 7 (2015) 23685–23693.
[23] X. Fan, X. Ji, F. Han, J. Yue, J. Chen, L. Chen, T. Deng, J. Jiang, C. Wang, Sci. Adv. 4 (2018), eaau9245.
[24] X. Han, Y. Gong, K.K. Fu, X. He, G.T. Hitz, J. Dai, A. Pearse, B. Liu, H. Wang, G. Rubloff, Nat. Mater. 16 (2017) 572–579.
[25] C. Yang, H. Xie, W. Ping, K. Fu, B. Liu, J. Rao, J. Dai, C. Wang, G. Pastel, L. Hu, Adv. Mater. 31 (2019), 1804815.
[26] X. Zhang, Q. Xiang, S. Tang, A. Wang, X. Liu, J. Luo, Nano Lett. 20 (2020) 2871–2878.
[27] X.-B. Cheng, C.-Z. Zhao, Y.-X. Yao, H. Liu, Q. Zhang, Chem 5 (2019) 74–96.
[28] F. Han, J. Yue, X. Zhu, C. Wang, Adv. Energy Mater. 8 (2018), 1703644.
[29] H. Huo, Y. Chen, J. Luo, X. Yang, X. Guo, X. Sun, Adv. Energy Mater. 9 (2019), 1804004.
[30] R. Schlenker, D. Stępień, P. Koch, T. Hupfer, S. Indris, B. Roling, V. Miß, A. Fuchs, M. Wilhelmi, H. Ehrenberg, ACS Appl. Mater. Interfaces 12 (2020) 20012–20025.
[31] H. Yan, H. Wang, D. Wang, X. Li, Z. Gong, Y. Yang, Nano Lett. 19 (2019) 3280–3287.
[32] M. Wang, J.B. Wolfenstine, J. Sakamoto, Electrochim. Acta 296 (2019) 842–847.
[33] X. Zhang, A. Wang, X. Liu, J. Luo, Acc. Chem. Res. 52 (2019) 3223–3232.
[34] Z. Hong, V. Viswanathan, ACS Energy Lett. 3 (2018) 1737–1743.
[35] J. Gao, D. Xue, W. Liu, C. Zhou, X. Ren, Actuators 6 (2017) 24.
[36] L. Fan, S. Li, L. Liu, W. Zhang, L. Gao, Y. Fu, F. Chen, J. Li, H.L. Zhuang, Y. Lu, Adv. Energy Mater. 8 (2018), 1802350.
[37] C.-J. Huang, B. Thirumalraj, H.-C. Tao, K.N. Shitaw, H. Sutiono, T.T. Hagos, T.T. Beyene, L.-M. Kuo, C.-C. Wang, S.-H. Wu, Nat. Commun. 12 (2021) 1–10.
[38] F. Han, A.S. Westover, J. Yue, X. Fan, F. Wang, M. Chi, D.N. Leonard, N.J. Dudney, H. Wang, C. Wang, Nat. Energy 4 (2019) 187–196.
[39] G. Liu, W. Weng, Z. Zhang, L. Wu, J. Yang, X. Yao, Nano Lett. 20 (2020) 6660–6665.
[40] F. Orsini, A. Du Pasquier, B. Beaudouin, J. Tarascon, M. Trentin, N. Langenhuizen, E. De Beer, P. Notten, J. Power Sources 81 (1999) 918–921.
[41] F. Orsini, A. Du Pasquier, B. Beaudoin, J. Tarascon, M. Trentin, N. Langenhuizen, E. De Beer, P. Notten, J. Power Sources 76 (1998) 19–29.
[42] H. Liu, X.-B. Cheng, J.-Q. Huang, H. Yuan, Y. Lu, C. Yan, G.-L. Zhu, R. Xu, C.-Z. Zhao, L.-P. Hou, ACS Energy Lett. 5 (2020) 833–843.
[43] W.D. Richards, L.J. Miara, Y. Wang, J.C. Kim, G. Ceder, Chem. Mater. 28 (2016) 266–273.
[44] J.A. Lewis, J. Tippens, F.J.Q. Cortes, M.T. McDowell, Trends in Chemistry 1 (2019) 845–857.
[45] C. Yu, Y. Li, K.R. Adair, W. Li, K. Goubitz, Y. Zhao, M.J. Willans, M.A. Thijs, C. Wang, F. Zhao, Nano Energy 77 (2020), 105097.
[46] X.-B. Cheng, R. Zhang, C.-Z. Zhao, Q. Zhang, Chem. Rev. 117 (2017) 10403–10473.
[47] J. Auvergniot, A. Cassel, J.-B. Ledeuil, V. Viallet, V. Seznec, R. Dedryvère, Chem. Mater. 29 (2017) 3883–3890.
[48] J. Zhang, C. Zheng, L. Li, Y. Xia, H. Huang, Y. Gan, C. Liang, X. He, X. Tao, W. Zhang, Adv. Energy Mater. 10 (2020), 1903311.
[49] F.J. Simon, M. Hanauer, F.H. Richter, J.r. Janek, ACS Appl. Mater. Interfaces 12 (2020) 11713–11723.
[50] F. Walther, R. Koerver, T. Fuchs, S. Ohno, J. Sann, M. Rohnke, W.G. Zeier, J.r. Janek, Chem. Mater. 31 (2019) 3745–3755.
[51] S. Wenzel, D.A. Weber, T. Leichtweiss, M.R. Busche, J. Sann, J. Janek, Solid State Ionics 286 (2016) 24–33.
[52] K.N. Wood, K.X. Steirer, S.E. Hafner, C. Ban, S. Santhanagopalan, S.-H. Lee, G. Teeter, Nat. Commun. 9 (2018) 1–10.
[53] N. Wu, Y. Li, A. Dolocan, W. Li, H. Xu, B. Xu, N.S. Grundish, Z. Cui, H. Jin, J.B. Goodenough, Adv. Funct. Mater. 30 (2020), 2000831.
[54] C. Wagner, W. Riggs, L. Davis, J. Moulder, G. Muilenberg, MN 1978..